

Optoelectronic and structural properties of amorphous silicon-carbon alloys deposited by low-power electron-cyclotron resonance plasma-enhanced chemical-vapor deposition

J. P. Conde

Department of Materials Engineering, Instituto Superior Técnico (IST), Avenue Rovisco Pais, 1096 Lisbon, Portugal

V. Chu

Instituto de Engenharia de Sistemas e Computadores (INESC), Rua Alves Redol 9, 1000 Lisbon, Portugal

M. F. da Silva

Instituto Tecnológico e Nuclear (ITN), Estrada Nacional n°10, 2685 Sacavem, Portugal

A. Kling, Z. Dai, and J. C. Soares

Centro de Física Nuclear da Universidade de Lisboa (CFNUL), Avenue Professor Gama Pinto 2, 1699 Lisbon, Portugal

S. Arekat

Physics Department, College of Science, University of Bahrain, P.O. Box 32038, State of Bahrain

A. Fedorov and M. N. Berberan-Santos

Centro de Química-Física Molecular, Instituto Superior Técnico (IST), Avenue Rovisco Pais, 1096 Lisbon, Portugal

F. Giorgis and C. F. Pirri

Department of Physics and INFN, Politecnico di Torino, Corso Duca degli Abruzzi 24, 10129 Torino, Italy

(Received 25 August 1998; accepted for publication 7 December 1998)

The optoelectronic and structural properties of hydrogenated amorphous silicon-carbon alloys (*a*-SiC:H) are studied over the entire compositional range of carbon content. The films are prepared using low-power electron-cyclotron resonance (ECR) plasma-enhanced chemical vapor deposition. The carbon content was varied by using different methane (or ethylene-)to-silane gas phase ratios and by introducing the methane (or ethylene) either remotely into the plasma stream or directly through the ECR source, together with the excitation gas (hydrogen). Regardless of the deposition conditions and source gases used, the optical, structural and transport properties of the *a*-SiC:H alloys followed simple universal dependencies related to changes in the density of states associated with their structural disorder. The deep defect density from photothermal deflection spectroscopy, the ESR spin density, the steady state and the transient photoluminescence, the dark and photoconductivity, the temperature of the hydrogen evolution peaks and the bonding from infrared spectroscopy are correlated to the Urbach tail energy, the *B* factor of the Tauc plot and E_{04} (defined as the energy at which the absorption coefficient is equal to 10^4 cm^{-1}). Silicon-rich and carbon-rich regions with very different properties, corresponding approximately to carbon fractions below and above 0.5, respectively, can be distinguished. The properties of the ECR *a*-SiC:H alloys are compared with those of alloys deposited by rf glow discharge. © 1999 American Institute of Physics. [S0021-8979(99)00606-4]

I. INTRODUCTION

Amorphous hydrogenated silicon-carbon alloys (*a*-SiC:H) are wide-band gap, thin-film semiconductors.¹ Alloys with low carbon content have been studied for many years and are used presently as transparent doped layers in single-junction solar cells and photodetectors and as the high-band gap window component in tandem solar cells. *a*-SiC:H alloys with high band gap (and high carbon content) emit visible photoluminescence at room temperature.^{2,3} This has led to studies of this material for application as the active layer in large-area electroluminescent devices.⁴⁻⁶ A more recent electronic application of high gap *a*-SiC:H alloys is thin-film cathodes for field emission displays.⁷

In electron cyclotron resonance (ECR) plasma-enhanced chemical vapor deposition (PECVD) the frequency of an input power source (usually in the microwave range) is matched to the cyclotron frequency set by a magnetic field in a resonant chamber. When this matching occurs, electrons absorb energy resonantly from the exciting electric field. ECR plasmas are usually operated at low pressure (<10 mTorr) with the ECR resonant chamber placed at some distance away from the substrate. Low-pressure operation results in the decomposition of source gas molecules by collisions with high-energy non-Maxwellian electrons, forming a high density stream of charged species.^{8,9} In the more widely used capacitively coupled rf glow discharge at 13.56 MHz,

high plasma densities result in high energy ions which can cause damage to the growing surface and interfaces. Higher frequency plasmas such as ECR generate a low energy (~ 30 eV) ion flux at the film surface.^{10,11} Since, in ECR, the ion energy is low, the energy at which ions impinge on the surface can be controlled independently of the microwave power by applying a bias to the substrate electrode.¹⁰ Furthermore, the low deposition pressures avoid polymerization by reducing the number gas-phase collisions and allow for sharper interfaces.

Hydrogenated amorphous silicon (*a*-Si:H) and *a*-SiC:H alloys are usually prepared using capacitively coupled rf glow discharge of silane and carbon source gases (e.g., methane, acetylene, ethylene). The deposition is typically performed at pressures above 50 mTorr in order to obtain a steady rf discharge. An alternative preparation technique for *a*-Si:H was demonstrated by Watanabe *et al.*,¹² who used a plasma stream of hydrogen containing high energy electrons coming from an ECR chamber to decompose silane. This plasma stream was introduced into the main chamber, to deposit *a*-Si:H at high growth rates ($3\text{--}15$ Å/s). The deposition of *a*-Si:H using an ECR plasma is usually performed at pressures below 10 mTorr and a high ion flux impinges on the growing surface.^{9,13–18} ECR was soon recognized to be a promising technique to prepare *a*-SiC:H alloys since the high-energy electrons generated by this technique are expected to be able to break the C–H bond of the source gases with more ease than the lower energy rf electrons, while at the same time avoiding the formation of graphite due to ion bombardment and impingement of atomic hydrogen.¹⁹ Liu *et al.* reported the deposition of amorphous silicon carbon alloys, *a*-SiC:H, and microcrystalline β -silicon-carbide, μc - β -SiC, by ECR from mixtures of H₂, CH₄ and SiH₄.²⁰ μc -SiC:H films, composed of silicon microcrystals embedded in an *a*-SiC:H matrix, have also been prepared by ECR at 5 mTorr and $T_{\text{sub}} = 300$ °C.^{21,22} Wide band gap, *p*-type and *n*-type doped, μc -SiC:H films were prepared from silane, methane and hydrogen by ECR at a pressure of 7.4×10^{-4} Torr, showing high dark conductivity and wide optical band gap.^{23,24} Doped μc -SiC:H films prepared by ECR have been applied to light emitting diodes (LEDs)^{21,23} and solar cells.²⁴ The effect of hydrogen dilution on *a*-SiC:H deposited by ECR from a 1:9 mixture of silane and acetylene was studied.²² Boron-doped *a*-SiC:H films with E_{04} between 2.0 and 2.35 eV deposited using ECR have been studied as a function of the microwave power.⁷ In this study, microcrystalline silicon formation was observed when high microwave powers were used, while for very high powers (>800 W), diamond-like phases were observed by Raman.⁷

The optical, electronic and structural properties of *a*-SiC:H alloys prepared by low-power (150 W) ECR PECVD are systematically studied. These properties are compared to those obtained for *a*-SiC:H deposited using standard rf glow discharge. Two carbon source gases (methane and ethylene) are used. *a*-SiC:H alloys covering the full compositional range up to *a*-C:H are prepared using both remote (by hydrogen excitation) and direct activation of methane and ethylene. In this study, the substrate tempera-

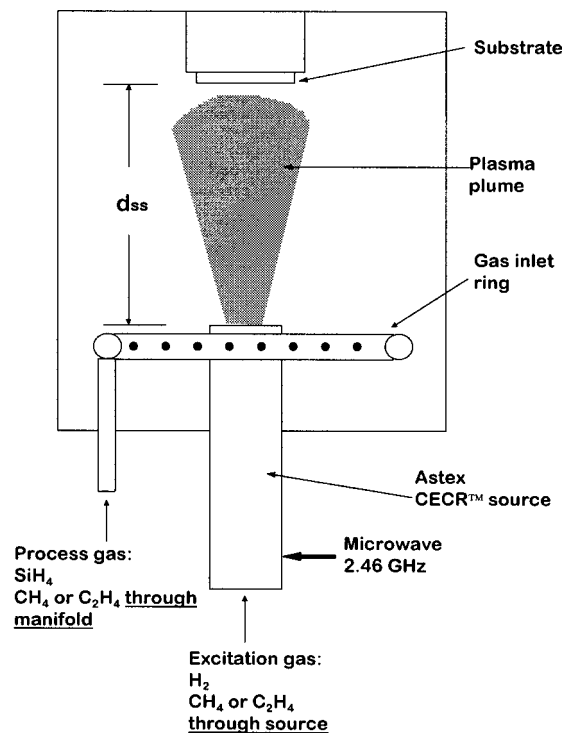


FIG. 1. Schematic diagram of the ECR-CVD deposition system.

ture, deposition pressure and hydrogen dilution were kept fixed.

II. EXPERIMENTAL PROCEDURES

A. Film preparation

The films were deposited by ECR-PECVD in an ultrahigh-vacuum system using an Astex-CECR source (Fig. 1). The excitation gas was introduced into a quartz resonance chamber which was surrounded by a water-cooled magnet coil. The microwave power (2.45 GHz) was coupled into this resonance chamber. The current through the magnet coil was adjusted to give the required magnetic field to achieve the ECR condition, resulting in a bright plasma plume emanating from the source. The mouth of the ECR source was placed at a distance (d_{ss}) of 6 cm from the substrate in the main chamber. The substrate was clamped to a grounded electrode heated to the deposition temperature of 200 °C. The pressure was kept at 10 mTorr. The power was kept constant at 150 W, which is in the low microwave power range. A hydrogen dilution of 95% was used throughout this work in order to prevent back flow of gas from the main chamber into the resonance chamber. The total flux of silane and carbon-source gas was kept constant at 1.5 sccm. Hydrogen was used as an excitation gas and was always introduced through the source while silane was always introduced directly into the main chamber via a ring-shaped gas distribution manifold with a diameter of 12.5 cm. A small flux of Ar (about 3% of the H₂ flux) was added along with the hydrogen in order to maintain a stable discharge. In order to study the effects of alloying with carbon two carbon source gases: methane (CH₄) and ethylene (C₂H₄) were used. The carbon-

containing gases, methane or ethylene, were introduced either through the manifold or through the source (as part of the excitation gas mixture with hydrogen).

For comparison, *a*-SiC:H films were also deposited by capacitively coupled radio frequency (rf) (13.56 MHz) PECVD in a parallel plate configuration in the same reactor. The deposition conditions were: substrate temperature of 200 °C, a deposition pressure of 0.1 Torr and a rf power of 10 W (~100 mW/cm²). Details about these samples can be found elsewhere.⁴

For each sample, films were deposited on two different substrates simultaneously: (1) Corning 7059 glass, for optical transmission, parallel transport measurements, photothermal deflection spectroscopy and Raman spectroscopy; (2) double-side-polished <100> Si, for infrared (IR) spectroscopy, photoluminescence and hydrogen evolution measurements. Selected samples were also deposited on Pyrex for ESR characterization.

B. Film characterization

The band gap of the films is determined optically by transmission measurements. The Tauc band gap E_{opt} was extracted from $(\alpha E)^{1/2} = B^{\text{Tauc}}(E - E_{\text{opt}})$, where the B factor of the Tauc plot is a constant, α is the absorption coefficient and E is the photon energy. For high carbon content (high-band gap) samples, however, the Tauc method is difficult to interpret because the linear region used for fitting the Tauc formula is reduced and because of the very wide band tails. For this reason in all samples E_{04} , which is defined as the energy where the absorption coefficient is equal to 10⁴ cm⁻¹, was also obtained from transmission measurements. Photothermal deflection spectroscopy (PDS) was used to measure the subgap absorption.²⁵ The PDS spectra were normalized to the absorption spectra measured by transmission. The Urbach energy E_u was extracted from a fit of the exponential tail of the PDS spectrum to $\alpha = \alpha_0 \exp[(E - E_0)/E_u]$, where α_0 and E_0 are constants.

Photoconductivity σ_{ph} was measured on coplanar Cr contacts with 6 mm length, 1 mm separation, and approximately 1000 Å thickness. The light from a 250 W tungsten-halogen lamp is passed through a bandpass filter, the wavelength of which depends on the band gap of the film and is chosen to ensure approximately uniform carrier generation throughout the thickness of the film. The generation rate is calculated from the response of a calibrated Si photodiode located next to the sample. For the purpose of comparison between samples, σ_{ph} measured at a carrier generation rate G of 10²¹ cm⁻³ s⁻¹ is quoted. Dark conductivity σ_d was measured in a perpendicular configuration (metal/*a*-SiC:H/metal or doped-crystalline silicon/*a*-SiC:H/metal).

The ion beam analysis measurements were performed using a 3.1 MV Van de Graaff accelerator. The Si/C ratios were determined by Rutherford backscattering spectrometry (RBS) of 2.0 MeV He⁺ ions for most of the films.²⁶ For samples with C contents too low for detection by RBS the elastic scattering resonance of protons at 1.75 MeV was used to enhance sensitivity.²⁷ In both cases the spectra of backscattered ions were recorded using surface barrier detectors

located at 160° and 180° with respect to the incoming beam in the Cornell geometry. The spectra were analyzed using the standard software RUMP for RBS²⁸ and SENRAS²⁹ for resonant scattering in order to obtain the Si/C ratios.

Room-temperature electron-spin resonance (ESR) measurements in the X band on films on Pyrex substrates were used to evaluate the density of unpaired spins. The detection limit in the evaluation of spin density was below 10¹⁷ spins/cm³. The incident power was less than 1 mW in order to prevent saturation. Both g values and the density of spins were obtained by comparison with standard samples.

Photoluminescence (PL) was measured to study the radiative recombination properties. Steady-state PL measurements were performed at room temperature with a SPEX Fluorolog system. Ultraviolet (UV) light from a Xe arc lamp is focused onto the sample through a 0.22 m monochromator with a 1.25 mm slit (giving an excitation bandwidth of 4.5 nm). The sample is placed at an angle of approximately 50°–75° with respect to the incident excitation light. The resulting photoluminescence is collected by a 0.22 m double monochromator with a 1.25 mm slit (giving an emission bandwidth of 2.25 nm) coupled with a photomultiplier tube. Picosecond time-resolved luminescence intensity decays were obtained by the single-photon timing method with excitation at 310 nm from a Coherent 701-2 laser, delivering 3–4 ps pulses (~40 nJ/pulse) at a frequency of 3.4 MHz. Detection by a microchannel plate photomultiplier was performed by passing the emission through a depolarizer and then through a Jobin-Yvon HR320 monochromator. The instrument response function had an effective full width half maximum (FWHM) of 30–40 ps. The decays were best fitted by a sum of three exponential decays. The average decay time is the weighted average of the decay times of the three exponential decays.

Infrared spectra were measured using a Nicolet Fourier transform infrared (FTIR) spectrometer. The results are quoted for the integrated absorption, $\int \alpha/\omega d\omega$, of a given band. Infrared spectroscopy has been extensively used to study the bonding in *a*-SiC:H alloys. Table I summarizes the assignments generally associated with some of the bands commonly observed.

Hydrogen evolution measurements were performed in a turbopumped high-vacuum apparatus having a base pressure of 4 × 10⁻⁹ Torr. The samples rested in a metal-sealed quartz tube which was placed inside a tube furnace. A thermocouple was used to measure the sample temperature and a constant heating rate of 5 °C/min was used. Hydrogen partial pressure was measured with a quadrupole mass analyzer, which was also used to monitor variations in the pumping speed of the turbopump by recording the pressure of an inactive gas, whenever needed. Rates of hydrogen evolution from the films were obtained from the pressure thermographs and were normalized to per unit volume of film.

III. RESULTS

A. Deposition rate and film composition

Figure 2 shows the deposition rate r_d as a function of the ratio of the flux of silane to that of methane or ethylene.

TABLE I. Summary of IR absorption band assignments.

Band (cm ⁻¹)	Modes	References
630	Si-H wagging	51
670	(1) Si-H _n wagging (2) Si-C stretching (3) both	35,52 51,53 1,37
770	(1) Si-C stretching (2) Si-CH ₃ rocking or wagging (3) Si-CH ₃ stretching	35,51,52 1,37,51,52,53 22,37
850-890	Si-H _n bending	51,54
1000	CH _n wagging and/or rocking	1,22,35,37,52
1600	sp ² C=C stretching	53
2000	Si-H stretching	37,52
2100	Si-H ₂ stretching	22,35,37,52
2870	sp ³ CH ₃ (symmetrical)	47
2900	sp ³ C-H _{2,3} stretching	1,35,37,55
2920	sp ³ CH ₂ (asymmetrical)	47,48
2956	sp ² CH ₂ (olefinic)	47
3045	sp ² C-H stretching	48,55

When the carbon source gas is introduced through the manifold [Fig. 2(a)] r_d decreases with decreasing flow of silane, saturating at $r_d \sim 0.2 \text{ \AA/s}$ for silane to carbon source gas ratios below 0.25. The values of r_d are similar for both carbon source gases when the gas flow ratio is above unity, and about 50% higher for ethylene than for methane for gas flow ratios below unity. r_d shows a very different behavior when the methane or the ethylene is introduced through the ECR source as part of the excitation gas mixture [Fig. 2(b)]. In this case, the values of r_d for gas flow ratios below unity

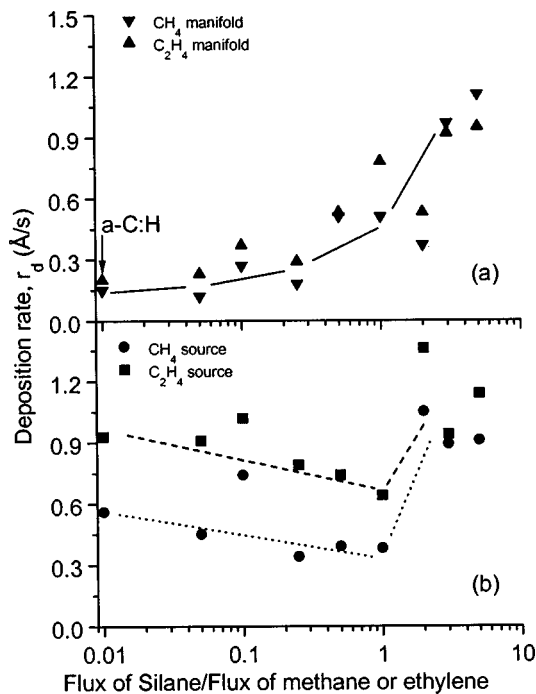


FIG. 2. Deposition rate r_d plotted as a function of the gas flow ratio of silane-to-methane or ethylene: (a) samples deposited with the methane or ethylene introduced through the gas manifold; (b) samples deposited with the methane or ethylene introduced through the ECR source. In both (a) and (b) the leftmost samples are a-C:H and were prepared without the addition of silane.

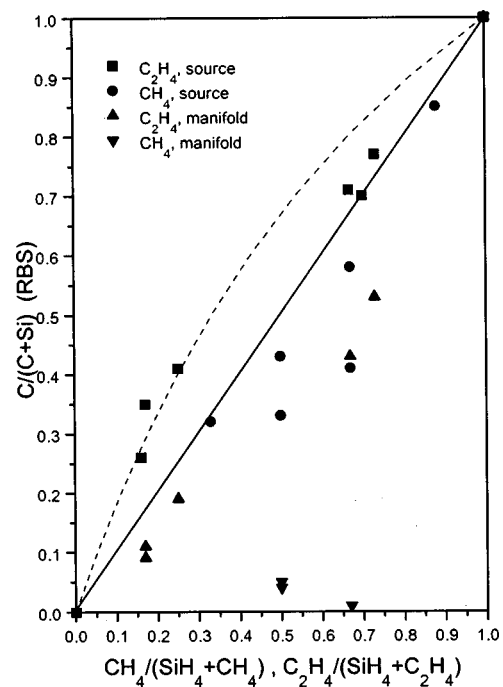


FIG. 3. Carbon atomic fraction ($C/C+Si$) in the a-SiC:H alloys measured using RBS, as a function of the gas phase flow ratio of methane or ethylene to the sum of the flows of silane and methane or ethylene. The solid and the dashed line indicate the carbon atomic fraction expected if the ratio of the silicon-to-carbon atoms in the gas phase is kept in the solid phase for methane and ethylene-containing gas mixtures, respectively.

remain approximately constant and are approximately two times higher for films deposited using ethylene than for films deposited using methane. For the same gas flow ratios below unity, r_d is higher for films deposited with the carbon-source gas introduced through the ECR source than for films deposited with the carbon-source gas introduced into the deposition chamber via the gas manifold.

Due to the introduction of carbon-source gases through the source, significant carbon deposition occurred inside the resonance chamber of the ECR source. This was also true even when the carbon-source gases were introduced into the deposition chamber via the gas manifold due to methane or ethylene backflow. In both cases, silane backflow contributes to silicon deposition inside the ECR source. This deposition inside the source resulted in an increasing reflection of the input microwave power with accumulated deposition time and eventually caused the plasma to turn off. Consequently, the values of r_d obtained for each sample showed some dependence on the ECR chamber history prior to deposition and this explains the scatter observed in Fig. 2. A postdeposition cleaning discharge of Ar/H_2 was found to significantly increase the time between shutdowns.

The carbon atomic fraction ($x = C/(C+Si)$) in the a-SiC:H alloy films, plotted as a function of the corresponding gas phase flow ratio of methane or ethylene to the sum of the flows of silane and methane or ethylene, is shown in Fig. 3. Also shown are the expected carbon atomic fractions in the film if the gas phase fraction of carbon to silicon atoms is preserved in the solid phase (solid line for methane-containing gas mixtures, dashed line for ethylene-containing

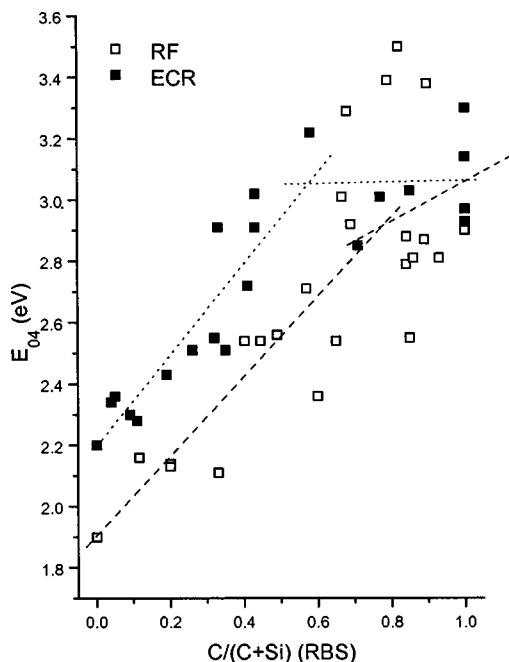


FIG. 4. Band gap E_{04} as a function of the carbon fraction in the film ($x = C/(C+Si)$) from RBS. Also shown, for comparison, are results for a -SiC:H deposited using rf glow discharge (open symbols). Linear regressions of the data are shown for ECR (dotted line) and rf (dashed line) samples. These linear regressions were calculated for $x < 0.5$ and $x > 0.6$.

gas mixtures). Figure 3 shows that the atomic fraction of carbon to silicon atoms in the gas phase is approximately the same as that fraction in the film when the methane or the ethylene are introduced through the ECR source. When the ethylene or the methane is introduced through the manifold the atomic fraction of carbon to silicon atoms in the film is smaller than the same fraction in the gas phase. In particular, when the methane is introduced through the manifold, there is essentially no incorporation of carbon in the film up to a methane to a total gas flow ratio of 0.7.

Figure 3 strongly suggests that when the methane or ethylene is introduced through the ECR source, there is enhanced direct excitation of the carbon-containing molecules by the ECR electrons in the ECR resonance area. It is possible that when the carbon-source gas is introduced via the manifold, the formation of carbon growth precursors proceeds mainly via collisions of the methane or ethylene molecules with silane radicals created by ECR electrons. However, as the flux of silane approaches zero, a finite r_d is still observed in this case, indicating a contribution to film growth from gas precursors produced either directly by gas-phase collisions of the ethylene and methane molecules with the plume ECR electrons in the deposition chamber or in the ECR resonance area because of gas backflow.

B. Optical absorption

Figure 4 shows the optical band gap, E_{04} , as a function of the carbon atomic fraction ($C/(C+Si)$) in the a -SiC:H alloy films. A roughly linear correlation is observed between E_{04} and the carbon fraction in the film. This figure indicates that it is appropriate to use the band gap as an indication of

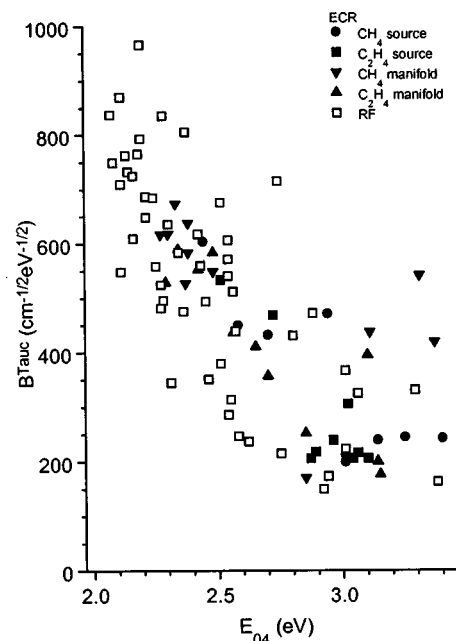


FIG. 5. B factor from the Tauc plot plotted as a function of the band gap E_{04} . Solid symbols are for ECR-deposited and open symbols for rf glow discharge-deposited a -SiC:H alloys.

the carbon content of the film. This assumption cannot be used for carbon atomic fractions above 0.6, for which a tendency to a saturation of the band gap at $E_{04} \geq 3$ eV is observed. The band gap of the a -SiC:H alloys deposited by ECR is systematically ~ 0.2 eV above the band gap of the a -SiC alloys deposited by rf glow discharge for carbon atomic fractions below 0.6, beyond which they are approximately the same.

Figure 5 shows that the B factor from the fit of the Tauc equation decreases with increasing E_{04} . The B factor has been previously taken as a measure of the structural disorder of the a -SiC:H films, in the sense that a higher value for B would indicate a lower degree of structural disorder.^{30,31} The B factor has also been related to the inverse of the conduction-band-tail width.³² Figure 5 shows that B decreases from a value $B \approx 800 \text{ cm}^{-1/2} \text{ eV}^{-1/2}$ at $E_{04} = 2.0$ eV (typical of unalloyed rf glow discharge a -Si:H) to a value $B \approx 150\text{--}300 \text{ cm}^{-1/2} \text{ eV}^{-1/2}$ for $E_{04} \geq 2.6$ eV. This last low value was attributed to a change of the band-edge character from Si-Si-like to C-C-like.³³ Figure 5 shows that the B factor for a -SiC:H deposited by ECR and by rf glow discharge follow approximately the same dependence on E_{04} . The a -SiC:H alloys which show photoluminescence visible with the naked eye at room temperature are those for which $B \leq 300 \text{ cm}^{-1/2} \text{ eV}^{-1/2}$. Figures 4 and 5, taken together, show that the values of B for a -SiC:H alloys deposited by ECR are $\sim 100 \text{ cm}^{-1/2} \text{ eV}^{-1/2}$ smaller than those for a -SiC:H alloys deposited by rf glow discharge for the same carbon fraction (for $x \leq 0.5\text{--}0.6$). For $x \geq 0.5\text{--}0.6$ both types of alloys show approximately the same value of B .

The subgap absorption spectrum of the a -SiC:H alloys prepared by ECR depends on the carbon content in the film. As the silane-to-methane or ethylene gas flow ratio is reduced, the absorption spectrum goes through a series of

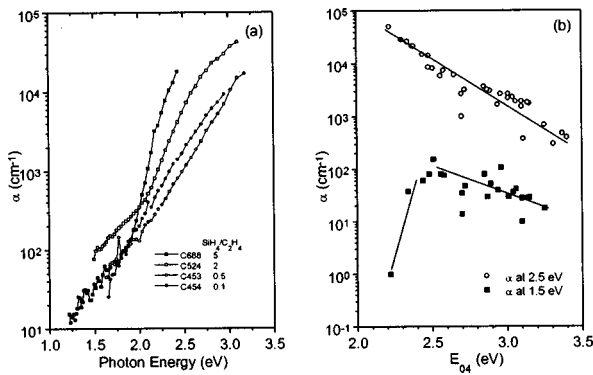


FIG. 6. (a) Absorption spectra measured by PDS- of ECR-deposited a -SiC:H alloys prepared by introducing ethylene into the deposition chamber different silane-to-ethylene gas flow ratios. (b) Absorption coefficient at 2.5 eV (open circles) and 1.5 eV (solid squares) plotted as a function of the band gap, E_{04} .

changes which are common to all four series of samples studied. These changes in the subgap absorption spectra depend only on the amount of carbon incorporated in the film: for Si-rich a -SiC:H alloys the subgap spectra have the same features as that of a -Si:H, with an exponential Urbach tail for energies below E_{04} and a deep defect absorption shoulder at lower energies [one example is the curve for sample C688 in Fig. 6(a)]; as the carbon content increases, the spectrum keeps the same overall shape but the Urbach tail becomes wider and the deep defect density increases [this can be seen for sample C524 in Fig. 6(a)]; as the carbon fraction increases beyond 0.5, the absorption spectra initially still shows an Urbach tail and a deep defect absorption shoulder but, while the Urbach tail width reaches a maximum value, the deep defect density decreases [in Fig. 6(a), this corresponds to sample C453]; finally, for the highest carbon content films the deep defect density shoulder is no longer observable and the absorption spectrum is approximately exponential [as can be seen for sample C454 in Fig. 6(a)]. Figure 6(b) shows the absorption coefficient at 2.5 eV [$\alpha(2.5$ eV)] and 1.5 eV [$\alpha(1.5$ eV)] as functions of E_{04} . While $\alpha(2.5$ eV) decreases exponentially with E_{04} , $\alpha(1.5$ eV) increases rapidly upon initial carbon incorporation, reaching a maximum around $E_{04} \approx 2.6$ eV. Above this value of E_{04} , $\alpha(1.5$ eV) decreases slowly with increasing E_{04} . 1.5 eV has been previously considered as the upper limit for the energy of the states responsible for nonradiative recombination because this is a value below which the room-temperature PL efficiency is negligible.³⁴

Figure 7 plots the Urbach energy E_u measured by PDS as a function of E_{04} . E_u increases roughly linearly with E_{04} up to 2.6 eV for rf a -SiC:H alloys and up to 2.8 eV for ECR a -SiC:H alloys and beyond that, it remains approximately constant around 225 ± 50 meV. For E_{04} above these values, which correspond to a carbon atomic fraction in the film of ≥ 0.5 , E_u remains well above 150 meV for all samples. Figures 4 and 7 taken together indicate that the dependence of E_u on the carbon content is independent of the technique used to deposit the film. It has been suggested that E_u is related to local structural disorder, while B is related to overall structural disorder.³¹ As would be expected from taking

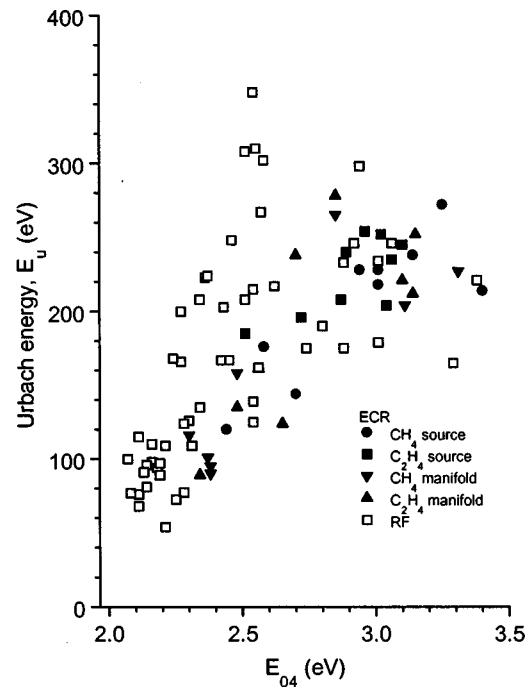


FIG. 7. Urbach energy E_u plotted as a function of the band gap E_{04} . Solid symbols are for ECR-deposited and open symbols for rf glow discharge-deposited a -SiC:H alloys.

Figs. 5 and 7 together, there is a linear correlation between E_u and the B factor of the Tauc plot which, from our results, gives the relation $E_u(\text{meV}) = 311 - 0.26B$ ($\text{cm}^{-1/2} \text{eV}^{-1/2}$) for the rf samples and a very similar $E_u(\text{meV}) = 303 - 0.29B$ ($\text{cm}^{-1/2} \text{eV}^{-1/2}$) for the ECR samples. This would suggest that the local defects related to microstructural disorder resulting from alloying with carbon dominate the overall defect structure of the film. Figures 5 and 7 suggest that the disorder of the network (as represented by the B factor of the Tauc plot and E_u , respectively) does not increase significantly above $C/(C+Si) \approx 0.5$. A change in the carbon environment has been previously proposed for carbon fractions ≥ 0.5 –0.6, in good agreement with the results shown in Fig. 7.^{35,36} For carbon atomic fractions smaller than 0.5, the carbon partially incorporates in the form of terminating configurations consisting of methyl (or ethyl) groups, longer polyethylene-like chains or in bridging configurations, with the dangling bonds being dominantly Si dangling bonds.³⁷ This occurs because the C–H bond is so strong (4.3 eV) that, at the substrate temperature used (200 °C), the H cannot redistribute to promote network formation. In this case, a non-equilibrium, kinetically limited growth results in a highly disordered structure. For carbon fractions above 0.5, the structure becomes polymer-like. In these films, C defects are dominant and, at a carbon fraction of 0.5–0.6, the onset of sp^2 sites forming π -bonded graphitic clusters has been predicted.³⁸ These π -bonded C clusters have a density of states symmetric around midgap³³ and could justify the saturation of the optical gap.

C. Dark and photoconductivity

Figure 8 shows that both σ_{ph} and σ_d of ECR and rf a -SiC:H alloys decrease exponentially with increasing E_{04} ,

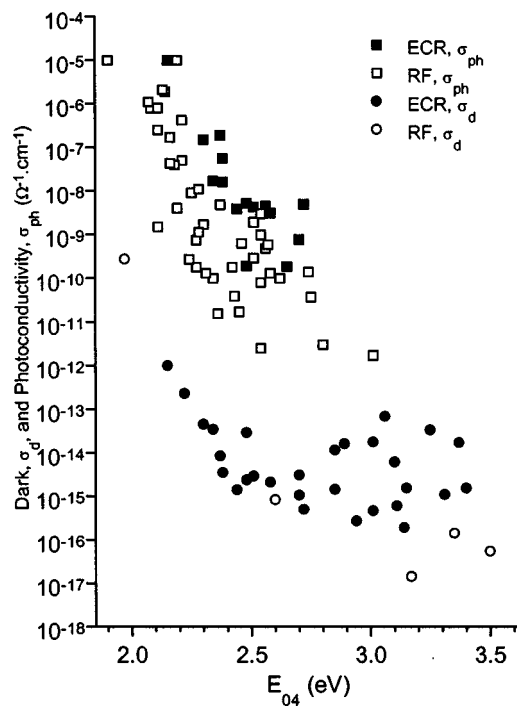


FIG. 8. Photoconductivity σ_{ph} (squares), and dark conductivity σ_d (circles) for ECR-deposited (solid symbols) and rf-deposited (open symbols) *a*-SiC:H alloys.

up to $E_{04} \sim 2.6\text{--}2.8$ eV, which corresponds roughly to a carbon atomic fraction of 0.5–0.6. The σ_{ph} decreases from 10^{-5} to $10^{-11} \Omega^{-1} \text{cm}^{-1}$ and σ_d decreases from 10^{-10} to $10^{-16} \Omega^{-1} \text{cm}^{-1}$. In this band gap range, the photo-to-dark photoconductivity ratio remains approximately constant at $\sim 10^5$. As the carbon content in the *a*-SiC:H alloys increases, the mobility-recombination lifetime product drops rapidly. For carbon atomic fractions below 0.5, a decrease of lifetime is expected due to the increase of E_u (Fig. 7) and, in consequence, an increase in the density of deep defects in the gap. In addition, an enhancement of the cross section of the recombination centers due to charging effects could also contribute to the lifetime decrease. For $E_{04} \geq 2.6\text{--}2.8$ eV, σ_{ph} is below our detection limit of around $10^{-11} \Omega^{-1} \text{cm}^{-1}$, and σ_d scatters between 10^{-14} and $10^{-17} \Omega^{-1} \text{cm}^{-1}$. This scatter may be due in part to errors in the perpendicular dark conductivity measurements caused possibly by small pinholes or shorts. For carbon atomic fractions above 0.5, a decrease of mobility is also possible if the carriers responsible for the photoconduction are no longer drifting at the mobility edge, but instead are hopping in the wide band tails. Different mechanisms could be envisioned for the dc conductivity of high-band gap *a*-SiC:H alloys, such as variable-range hopping, transport in band-tail states, hopping between graphite-like clusters or multiphonon tunneling.³⁹ The available transport data, taken at room temperature, do not allow us to draw any conclusion at this point.

D. Photoluminescence

Figure 9 shows the room-temperature, steady-state, (PL) emission spectra of representative ECR-deposited *a*-SiC:H alloys. The half width of the PL peak was relatively constant

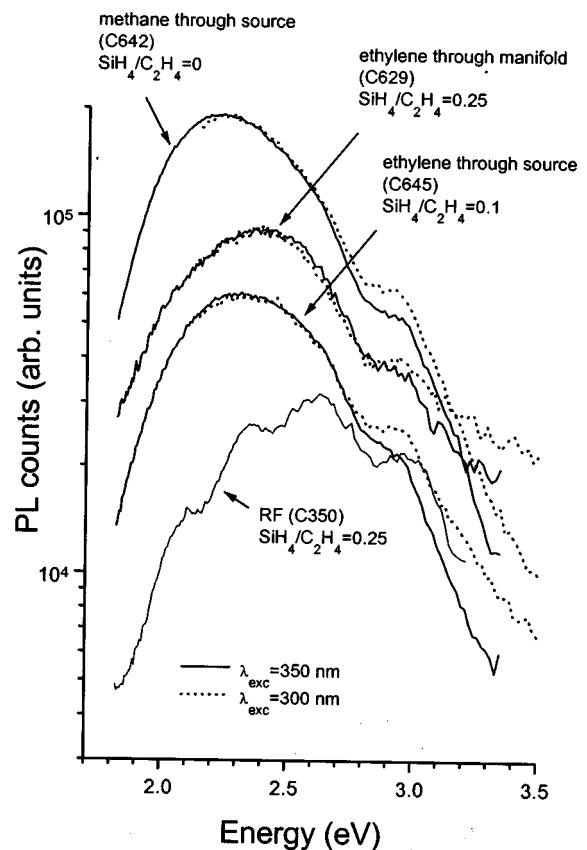


FIG. 9. Steady-state photoluminescence emission spectra, measured at room temperature, of representative *a*-SiC:H alloys deposited by ECR. Also shown, for comparison, is the spectrum for an *a*-SiC:H alloy prepared using rf glow discharge. All samples shown have $E_{04} \approx 3.0$ eV.

around 150 ± 25 nm for all samples that showed room-temperature PL in this visible range. No well defined characteristic line shape could be identified. The position of the luminescence peak was at essentially the same energy for all luminescent samples deposited using a given set of deposition conditions (i.e., for samples deposited using either ethylene through the source, ethylene through the manifold or methane through the source). The PL peak position falls ~ 0.6 eV below E_{04} and is centered around 2.3–2.4 eV. This is in contrast with the dependence of the peak position on E_{04} observed for rf-deposited *a*-SiC:H alloys.^{3,4} The data suggest a dependence of the PL peak energy on the deposition conditions: 2.35 eV for ECR *a*-SiC:H alloys deposited using methane through the source, 2.31 eV for alloys deposited using ethylene through the source, and 2.21 eV for alloys deposited using ethylene through the manifold. In general, samples deposited using methane through the manifold did not show strong visible PL.

Figure 10 shows the average decay time τ_{avg} of representative ECR-deposited *a*-SiC:H alloys. The alloys studied had a carbon content of approximately 0.8 and $E_{0,4} \approx 3.0$ eV. The decay times increase approximately linearly with decreasing emission energy and are in the range of 100–800 ps. The samples in which the methane was introduced through the source (C673) and the ethylene was introduced through the manifold (C629) have τ_{avg} approximately 200 ps higher than for the sample in which the ethylene was introduced

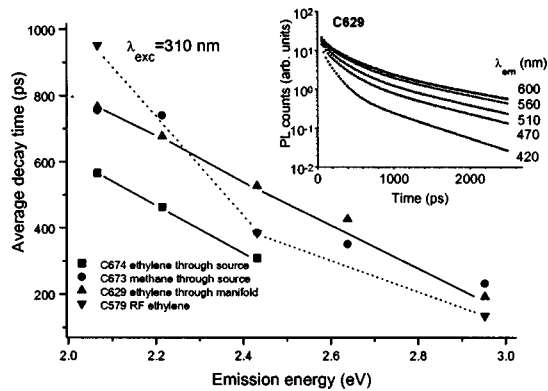


FIG. 10. Average decay time τ_{avg} as a function of the emission energy measured at room temperature. The inset illustrates the analytic approximation of the time-resolved PL excited at 4 eV for sample C629. Also shown for comparison is τ_{avg} for an a -SiC:H alloy prepared using rf glow discharge. All samples shown here have $E_{04} \approx 3.0$ eV.

through the source (C674). The a -SiC:H alloy prepared using rf glow discharge has a stronger dependence of τ_{avg} with the emission energy than the ECR a -SiC:H alloys. In both of the experiments reported in Figs. 9 and 10, the excitation energies are in the range of 3.5–4 eV. Figure 9 shows that there is no change in the steady-state PL emission in this range of excitation energies. The short decay times (below 1 ns) suggest that the optical excitation creates electron–hole pairs in strongly localized excited states, rather than above the mobility edge, where the carriers are free to diffuse and to find nonrecombination centers.^{40–42}

As mentioned above, for Si-rich a -SiC:H, the structure of the films is expected to be mainly a tetrahedrally coordinated amorphous network of Si–Si bonds, with the C atoms incorporated in a terminating or bridging configuration. In this case, the PL mechanism is expected to be similar to that observed in a -Si:H, in which tunneling between localized states is involved with long radiative lifetimes and a strong temperature dependence.⁴³ In this case, the main recombination channel is through the Si dangling bond. The ECR samples that show room-temperature PL are those which have carbon atomic fractions in the film above 0.5 (corresponding to $E_{0,4} > 2.7$ eV, $B < 300 \text{ cm}^{-1/2} \text{ eV}^{-1/2}$, $E_u > 150$ meV). At this high carbon fraction, the PL was attributed in rf a -SiC:H alloys to emission resulting from monomolecular recombination of the photogenerated electron and hole which are localized in the same region in real space and recombine radiatively. In this case, the PL shows short lifetime, weak temperature dependence and relatively high efficiency, and is not quenched by electric fields.^{36,44} The wide-band tails observed in these films should induce a fast thermalization which would reduce the influence of carrier diffusion and localize the photogenerated pair. The recombination would then correspond to the recombination of electron–hole pairs with completely overlapping wave functions forming a trapped exciton.⁴⁵ The localization would be helped by the small dielectric constant of the high-band gap a -SiC:H alloys (the index of refraction is around ~ 2). The range of emission energies in Fig. 10 (2–3 eV) corresponds to a region of rapidly varying density of states (Fig. 6). The increase in decay

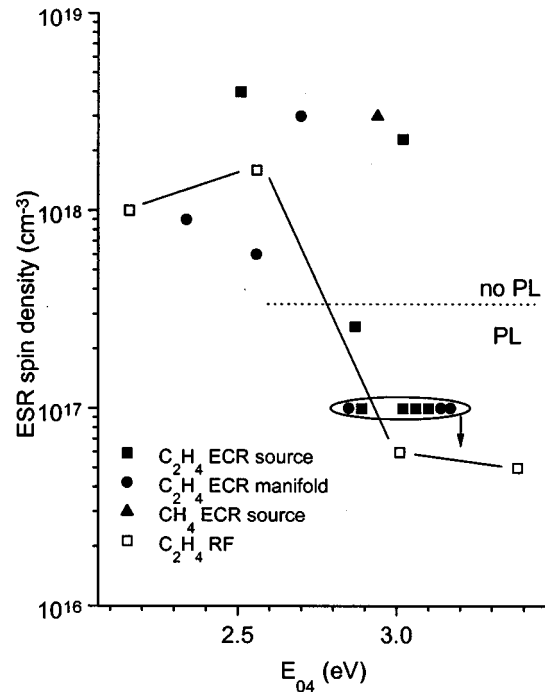


FIG. 11. ESR spin density plotted as a function of E_{04} . The encircled points correspond to samples whose spin densities were below the detection limit of 10^{17} cm^{-3} . The solid symbols are for a -SiC:H alloys deposited by ECR, while the open symbols are for films deposited using rf glow discharge.

times with decreasing emission energy may be due to a smaller rate of tunneling or hopping to neighboring states (nonradiative recombination) due to the smaller density of states available. The overall picture of PL emerging from Figs. 9 and 10 is similar in a -SiC:H alloys deposited by ECR and rf in agreement with their overall similar density of states in the gap, but the stronger dependence of the τ_{avg} on the emission energy and the dependence of the peak energy on the carbon content for rf samples suggests that details of the density of states may be different.

E. ESR

Figure 11 shows the ESR spin density of the a -SiC:H alloy as a function of E_{04} . This corresponds to the density of defects with an unpaired spin. Silicon-rich a -SiC:H alloys show spin densities $\sim 10^{18} \text{ cm}^{-3}$. As the E_{04} increases above 2.8 eV (corresponding to a carbon fraction > 0.5 –0.6), an abrupt decrease of the spin density to below 10^{17} cm^{-3} is observed. For this set of samples, only those whose ESR spin density was below $3 \times 10^{17} \text{ cm}^{-3}$ showed efficient room-temperature PL. In Fig. 11, the group of samples encircled had spin densities below the detection limit of the ESR and the upper limit of the spin density was plotted.

The states near the Fermi level control the nonradiative recombination processes of electrons and holes. In high-band gap a -SiC:H alloys, these states can be states arising from C π -state band tails, Si and C σ dangling bonds, C sp^2 isolated dangling bonds, and π states due to sp^2 clusters made up of an odd number of atoms (namely, fivefold and sevenfold aromatic rings).^{34,41,46} These nonradiative recombination centers can be ESR active and/or optically active.³⁴ A pro-

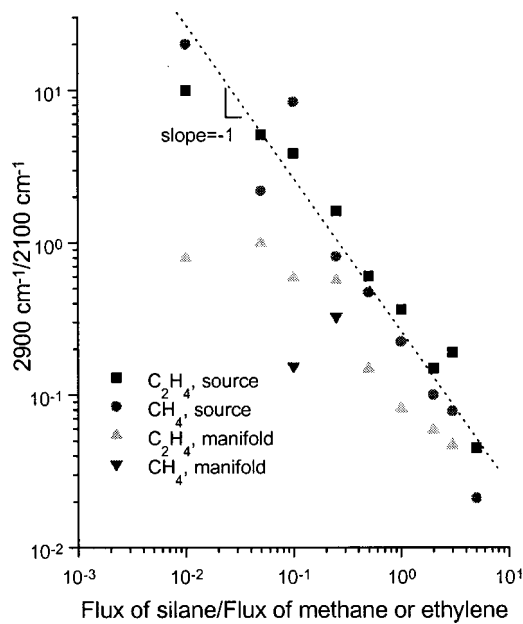


FIG. 12. The ratio of integrated absorption of the 2900 and 2100 cm^{-1} infrared (IR) absorption bands for ECR a -SiC:H alloys plotted as a function of gas flow ratio of silane-to-methane or ethylene.

portionality between $\alpha(1.5)$ and the density of nonradiative centers has been found for a -C:H films deposited by rf and sputtering. If this behavior is maintained for C-rich a -SiC:H films, since the density of nonradiative recombination centers {which is proportional to the optical absorption below 1.5 eV [Fig. 6(b)]} is larger than the ESR spin density, then ESR inactive centers located close to the Fermi level may be present and play a role in the nonradiative recombination.³⁴ Although the proportionality constant between $\alpha(1.5)$ and the density of nonradiative recombination centers is not known, the decrease in $\alpha(1.5)$ shown in Fig. 6(b) appears to be significantly slower than the decrease in ESR spin density. This suggests the predominance of optically active centers (tails of doubly occupied π states and sp^2 clusters with an odd number of atoms).

F. Infrared absorption

Figure 12 shows the ratio of integrated absorption of the 2900 and 2100 cm^{-1} IR absorption bands as a function of the flux of silane to the flux of methane or ethylene. The bands centered around 2900 and 2100 cm^{-1} are associated to vibrational stretching modes of carbon bonded to hydrogen and silicon bonded to hydrogen, respectively (Table I). An approximate inverse proportionality between the ratio of the 2900 and 2100 cm^{-1} bands and the ratio of the fluxes of silane and methane or ethylene is observed. To the extent that the ratio between these two bands reflects the carbon incorporation in the film, it can be observed that for the same gas flow ratio, the highest carbon fraction is incorporated when ethylene is introduced through the source, followed by methane through the source, ethylene through the manifold, and finally, methane through the manifold, in agreement with Fig. 3.

Figure 13 shows both (a) the ratio of integrated absorp-

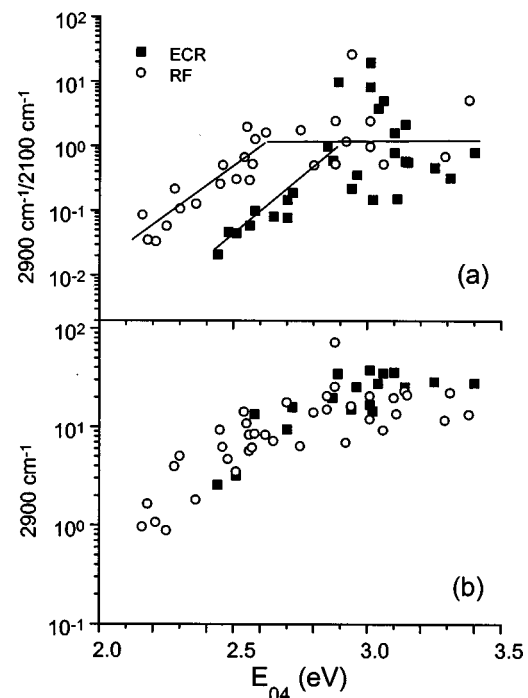


FIG. 13. (a) The ratio of integrated absorption of the 2900 and 2100 cm^{-1} infrared (IR) absorption bands for ECR a -SiC:H alloys plotted as a function of the band gap E_{04} . (b) The integrated absorption of the 2900 cm^{-1} band plotted as a function of the band gap, E_{04} . The solid symbols and the open symbols refer to ECR-deposited and rf-deposited a -SiC:H alloys, respectively.

tion of the 2900 and 2100 cm^{-1} IR absorption bands and (b) the integrated absorption of the 2900 cm^{-1} band as a function E_{04} . The 2900 cm^{-1} band has the same dependence on E_{04} for ECR and rf a -SiC:H alloys. There is an increase from ~ 1 to 20 cm^{-1} as E_{04} increases up to 2.8 eV, and it remains approximately constant for $E_{04} \geq 2.8$ eV. If the proportionality constant between the number of oscillators and the integrated absorption is chosen to be $1.35 \times 10^{21} \text{ cm}^{-2}$,⁴⁷ then the hydrogen concentrations bonded to C-H can be roughly estimated to vary between 2% and 50% for the a -SiC:H alloys studied. The 2900/2100 cm^{-1} ratio, on the other hand, is approximately the same (~ 1) for ECR and rf a -SiC:H alloys with $E_{04} \geq 2.8$ eV, decreasing with E_{04} for the ECR samples for $E_{04} < 2.8$ eV and for rf samples for $E_{04} < 2.6$ eV. This difference between ECR and rf disappears if, instead of E_{04} , the carbon fraction in the film is used (Fig. 4). The difference between Figs. 13(a) and 13(b) results from a higher absorption in the 2100 cm^{-1} band for ECR than rf a -SiC:H alloys, as can be seen in Fig. 14(b). For ratios of the 2900 and 2100 cm^{-1} bands smaller than 1, which, according to Fig. 13(a) correspond to $E_{04} < 2.8$ eV (which, according to Fig. 4, correspond to carbon contents below 0.5–0.6 and, according to Fig. 5, correspond to values of the B factor of the Tauc plot above $400 \text{ cm}^{-1/2} \text{ eV}^{-1/2}$), the ECR a -SiC:H alloys show significantly increased Si-H stretching absorption. Figure 14(a) shows that the integrated absorption for the 770 cm^{-1} band, which is associated with a Si-C vibrational mode (see Table I) has a maximum for a B factor of the Tauc plot of $\approx 400 \text{ cm}^{-1/2} \text{ eV}^{-1/2}$, corresponding to carbon fraction $x \sim 0.5$, decreasing for both lower and higher values of the 2900/2100

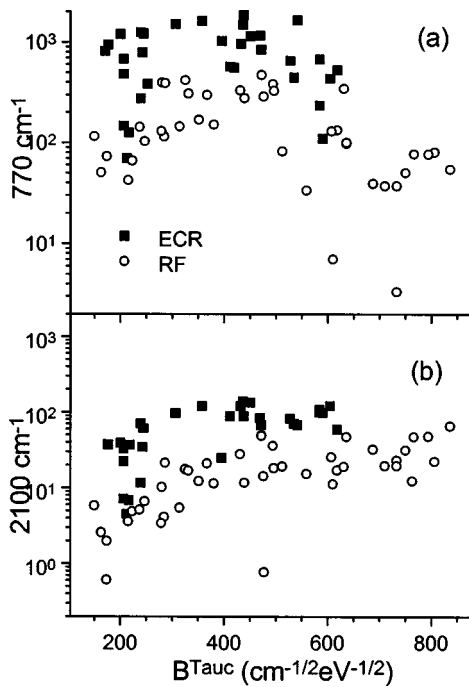


FIG. 14. (a) Integrated absorption of the 770 cm^{-1} IR absorption band and (b) integrated absorption of the 2100 cm^{-1} band plotted as a function of the B factor from the Tauc plot.

cm^{-1} ratio (and hence, for the high and low values of carbon atomic fraction in the film). Figure 14(a) shows that the Si–C absorption is significantly higher for ECR $a\text{-SiC:H}$ films, particularly in the Si-rich range.

No C–C or C–H sp^2 bonds were observed using FTIR. In particular, no significant absorption in the spectral range above 3000 cm^{-1} was observed. Raman spectroscopy did not reveal the presence of any C–C bonds. Both of these methods are limited in their sensitivity. One must keep in mind that a major drawback of IR analysis is that only those carbon atoms carrying at least one hydrogen atom are detectable. Nuclear magnetic resonance (NMR) investigations have shown that the amount of carbon not bonded to hydrogen can be as high as 65% and that hydrogen is preferably bound to sp^3 carbon.⁴⁸

G. Hydrogen evolution

Figure 15 shows characteristic hydrogen evolution spectra of ECR $a\text{-SiC:H}$ alloys. There is a main evolution peak (low- T peak) whose position shifts upward in temperature as the carbon fraction in the film increases. For the Si-rich films, a second evolution peak can be observed (high- T peak) which shifts to higher temperatures as the carbon fraction increases. This peak eventually leaves the measurement range ($T_{\text{max}}=900\text{ }^\circ\text{C}$). The low evolution temperatures observed suggest that the low- T peak results from desorption from voids or grain boundaries. The high- T peak could result from effusion from the bulk of the film, limited by the diffusion of atomic hydrogen.

Figure 16 shows the dependence of the hydrogen evolution peak position on E_{04} . The low- T peak position increases approximately linearly with E_{04} from 400 to $700\text{ }^\circ\text{C}$ for E_{04}

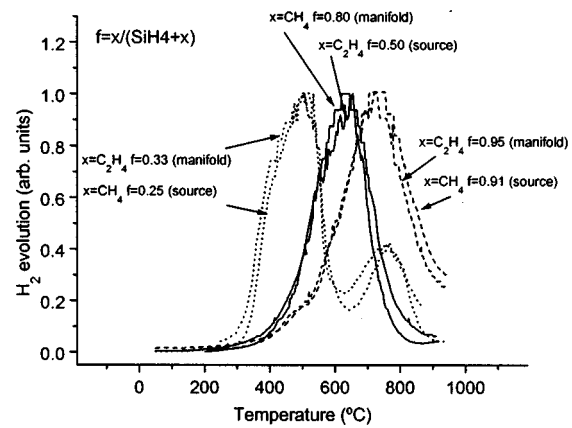


FIG. 15. Hydrogen evolution spectra of ECR $a\text{-SiC:H}$ alloys. Spectra shown are characteristic of Si-rich alloys ($x \leq 0.5$, open circles and squares), C-rich alloys ($x \geq 0.5$, open triangles) and alloys with a carbon fraction of ~ 0.5 (dark circles and squares).

$< 2.8\text{ eV}$, and remains constant around $700\text{ }^\circ\text{C}$ for $E_{04} \geq 2.8\text{ eV}$. The high- T peak starts at $\sim 600\text{ }^\circ\text{C}$ and reaches $800\text{ }^\circ\text{C}$ for $E_{04} \sim 2.6\text{ eV}$ before reaching the maximum temperature limit of the measurement apparatus. No difference could be observed between the rf and ECR $a\text{-SiC:H}$ alloys.

IV. DISCUSSION

The optical, structural and transport properties of $a\text{-SiC:H}$ alloys prepared using ECR over a wide range of deposition conditions were presented in Sec. III. The physical properties of the $a\text{-SiC:H}$ alloys are mainly determined by the silicon-to-carbon ratio, the hydrogen content of the films, and the silicon, hydrogen and carbon bonding configurations. In $a\text{-SiC:H}$ alloys, these factors are all closely con-

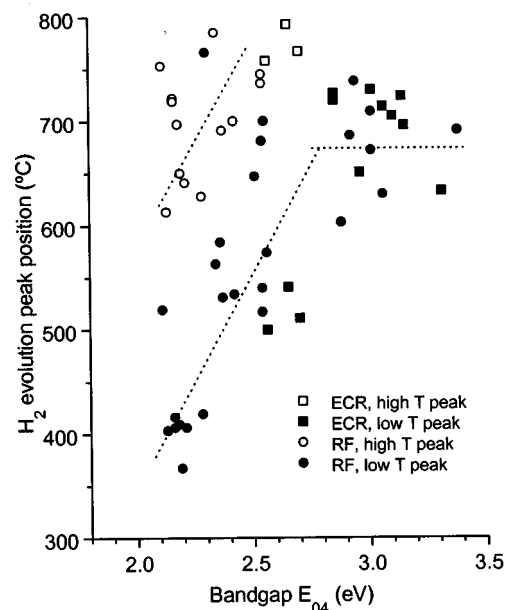


FIG. 16. H_2 evolution spectrum peak position as a function of the band gap E_{04} .

nected and determine the density of states of the *a*-SiC:H films. All the measured properties of the film correlate, at least partially, with the density of states.

rf-deposited *a*-SiC:H alloys with low carbon content have an Si sp^3 skeleton, with the carbon incorporated mostly in $-CH_3$ bond terminating configurations. However, when deposited by ECR, the increase in Si-C absorption observed by IR [Fig. 14(a)] and the lower carbon content for the same E_{04} relative to rf films (Fig. 4) indicate that additional carbon is incorporated substitutionally in the silicon matrix. As the carbon concentration increases to 0.5, a smooth transition occurs: E_{04} (Fig. 4), E_u (Fig. 7), the ESR spin density (Fig. 11), the temperature of the hydrogen evolution peak (Fig. 16), and the integrated absorption of the C-H stretching band (Fig. 13) increase, while the B factor of the Tauc plot (Fig. 5), σ_d (Fig. 8), and σ_{ph} (Fig. 8) decrease. With high carbon contents ($x \geq 0.5-0.6$), visible PL appears (Fig. 9) and these variables remain approximately constant all the way to *a*-C:H, independently of the Si concentration. This suggests that the density of states for $x \geq 0.5$ is controlled by the bonds formed by the carbon subskeleton. Most likely, the Si σ bonds are mostly with C and occur at higher energies. Other variables show a more gradual variation with the carbon content, such as the integrated absorption of the Si-C band [Fig. 14(a)], showing a maximum at $x \sim 0.5$ and the subgap optical absorption (Fig. 6, Sec. III B).

The ECR *a*-SiC:H alloys with $x \geq 0.5$ exhibit polymer-like characteristics such as a wide optical band gap and they exhibit intense room temperature photoluminescence in the visible range. Polymer-like *a*-C:H is softer than diamond-like carbon (DLC) because of their larger hydrogen content (50%–60% instead of 20%–30%). The polymer-like form has efficient photoluminescence because it is not hard enough to exhibit too many dangling bonds and not too soft to lose its excitation by self-distortion.⁴⁹

It is tempting to consider, for *a*-SiC:H alloys with high carbon content, the model developed for amorphous carbon (*a*-C:H), which is generally thought to consist of small C sp^2 -coordinated clusters embedded in a sp^3 -coordinated matrix. Tetrahedrally coordinated atoms (sp^3 hybrids) would allow three-dimensional crosslinking. In this model, graphitic clusters composed of π states of sp^2 -bonded carbon with π valence and π^* conduction states form the band edges determining the optical properties (such as the optical gap) since the σ - σ^* transitions occurs at much higher energies (>3 eV).^{34,41,46} A first consequence of this model is that the optical Tauc gap and E_{04} do not necessarily have a direct connection to the mobility gap.⁴⁶ In this model, the larger the clusters, the smaller the band gap. The relatively high band gap and the wide tails observed in Figs. 4–8 are compatible with a structure with small and numerous C sp^2 clusters in high-band gap *a*-SiC:H alloys, regardless of the deposition technique used (ECR or rf glow discharge). In the C sp^2 model, the Urbach energy may reflect the distribution of clusters, since the presence of the sp^2 clusters will give rise to strong potential fluctuations of the band edges.⁴⁰ The range of different cluster sizes and local gaps would cause the density of states to tail into the gap.

Alternatively, the polymer-like *a*-SiC:H alloys may consist of a single interacting system, rather than a set of weakly interacting clusters with their own internal states, and it may be more appropriate to treat it like a conventional amorphous semiconductor, with disorder-induced band tails, mobility edges and extended states.⁴¹

V. CONCLUSIONS

The optoelectronic and structural properties of hydrogenated amorphous silicon-carbon alloys (*a*-SiC:H) prepared by low-power ECR using hydrogen dilution and a grounded substrate were studied over the entire compositional range of carbon content. The carbon content was varied by using different methane (or ethylene)-to-silane gas phase ratios and by introducing the methane (or ethylene) either remotely into the plasma stream or directly through the ECR source, together with the excitation gas (hydrogen). Although the deposition rates and the carbon incorporation depended strongly on the mode of introduction of the carbon-source gas, no significant difference in the properties of the *a*-SiC:H alloys with the same band gap was observed. The properties of the ECR *a*-SiC:H alloys studied are comparable to those of alloys deposited by rf glow discharge with the same band gap. The most significant difference was the enhancement of the absorption bands at 2100 and 770 cm^{-1} , corresponding, respectively, to Si-H and Si-C vibrations observed in the ECR *a*-SiC:H alloys.

The atomic fraction of carbon to silicon atoms in the gas phase is approximately the same as that fraction in the film when the methane or the ethylene are introduced through the ECR source. When ethylene is introduced through the manifold the carbon incorporation in the film is reduced and is similar to that observed in rf glow discharge. When methane is introduced through the manifold the carbon incorporation in the film is strongly reduced and is below that observed in rf glow discharge. E_{04} increases approximately linearly with the carbon fraction in the film up to $x \sim 0.5-0.6$. For $x \geq 0.6$, a tendency toward a saturation of the band gap at $E_{04} \geq 2.8$ eV is observed. The Urbach tail energy E_u and the B factor of the Tauc plot correlate with E_{04} . Up to $E_{04} \sim 2.8$ eV, E_u increases monotonically from 50 up to ~ 200 meV, while the B factor decreases from ~ 800 down to ~ 200 $cm^{-1/2} eV^{-1/2}$. Above $E_{04} \sim 2.8$ eV, both E_u and B remain essentially constant. The deep defect density increases sharply with initial carbon incorporation, decreasing slowly for $x \geq 0.3$. The photoconductivity and the dark conductivity decrease exponentially with E_{04} and are below 10^{-11} and $\sim 10^{-15} \Omega^{-1} cm^{-1}$, respectively, when $E_{04} \geq 2.8$ eV. Visible room-temperature photoluminescence is observed when $E_{04} \geq 2.8$ eV. The photoluminescence peak position lies an average of 0.6 eV below the value of E_{04} . The decay times of photoluminescence increase approximately linearly with decreasing emission energy and are in the range of 100–800 ps. An abrupt decrease in the ESR spin density to below $10^{17} cm^{-3}$ is observed for carbon fractions greater than 0.5–0.6.

For possible applications of the wide-band gap *a*-SiC:H alloys, namely in electroluminescent devices, it is crucial to understand their carrier transport properties as well as the

contact properties of these films. In addition, the absorption rate of growth precursors on the substrate surface (namely SiH₃ and CH₃) depends strongly on the generation rate of dangling bonds, which depends on the ion bombardment and H-atom flux.⁵⁰ It is expected that deposition of *a*-SiC:H alloys by ECR under different conditions of hydrogen dilution and substrate bias could result in modification of the structure and properties.

ACKNOWLEDGMENTS

This work was supported by Fundação para a Ciência e Tecnologia (FCT) through pluriannual contracts with ICEMS and INESC and by Project No. PRAXIS/3/3.1/MMA/1901/95.

- ¹J. Bullo and M. P. Schmidt, *Phys. Status Solidi B* **143**, 345 (1987).
- ²D. Engemann, R. Fischer, and J. Knecht, *Appl. Phys. Lett.* **32**, 567 (1978).
- ³D. Kruangam, T. Endo, G. P. Wei, S. Nonomura, H. Okamoto, and Y. Hamakawa, *J. Non-Cryst. Solids* **77&78**, 1429 (1985).
- ⁴V. Chu, J. P. Conde, J. Jarego, P. Brogueira, J. Rodriguez, N. Barradas, and J. C. Soares, *J. Appl. Phys.* **78**, 3164 (1995).
- ⁵Y. Hamakawa, T. Toyama, and H. Okamoto, *J. Non-Cryst. Solids* **115**, 180 (1989).
- ⁶M. Yoshimi, H. Shimizu, K. Hattori, H. Okamoto, and Y. Hamakawa, *Optoelectron.—Devices Technol.* **7**, 69 (1992).
- ⁷S. F. Yoon, R. Ji, and J. Ahn, *Philos. Mag. B* **77**, 197 (1998).
- ⁸M. Azuma, T. Yokoi, I. Shiiya, and I. Shimizu, *J. Non-Cryst. Solids* **164–166**, 47 (1993).
- ⁹M. Zhang, Y. Nakayama, S. Nonoyama, and K. Wakita, *J. Non-Cryst. Solids* **164–166**, 63 (1993).
- ¹⁰R. G. Andosca, W. J. Varhue, and E. Adams, *J. Appl. Phys.* **72**, 1126 (1992).
- ¹¹R. E. Hollingsworth and P. K. Bhat, *Appl. Phys. Lett.* **64**, 616 (1994).
- ¹²T. Watanabe, M. Tanaka, K. Azuma, M. Nakatani, T. Sonobe, and T. Shimada, *Jpn. J. Appl. Phys., Part 1* **26**, 1215 (1987).
- ¹³J. Perrin, *J. Non-Cryst. Solids* **137&138**, 639 (1991).
- ¹⁴Y. Nakayama, K. Hitsuiishi, M. Zhang, H. Imamura, and T. Kawamura, *J. Non-Cryst. Solids* **137&138**, 669 (1991).
- ¹⁵J. P. Conde, V. Schotten, S. Arekat, P. Brogueira, R. Sousa, and V. Chu, *Jpn. J. Appl. Phys., Part 1* **36**, 38 (1997).
- ¹⁶S. Bae, A. K. Kalkan, S. Cheng, and S. J. Fonash, *J. Vac. Sci. Technol. A* **16**, 1912 (1998).
- ¹⁷W. C. Choi, E. K. Kim, S. K. Min, C. Y. Park, J. H. Kim, and T. Y. Seong, *Appl. Phys. Lett.* **70**, 3014 (1997).
- ¹⁸K. Erikson, V. L. Dalal, and G. Chumanov, *Mater. Res. Soc. Symp. Proc.* **467**, 409 (1997).
- ¹⁹A. von Keudell and W. Jacob, *J. Vac. Sci. Technol. A* **15**, 402 (1997).
- ²⁰C. C. Liu, C. Lee, K. L. Cheng, H. C. Cheng, and T. R. Yew, *Appl. Phys. Lett.* **66**, 168 (1995).
- ²¹T. Futagi, N. Ohtani, M. Katsuno, K. Kawamura, Y. Ohta, H. Mimura, and K. Kitamura, *J. Non-Cryst. Solids* **137&138**, 539 (1991).
- ²²S. F. Yoon and J. Ahn, *J. Vac. Sci. Technol. A* **15**, 1832 (1997).
- ²³D. Kruangam, T. Toyama, Y. Hattori, M. Deguchi, H. Okamoto, and Y. Hamakawa, *J. Non-Cryst. Solids* **97&98**, 293 (1987).
- ²⁴Y. Matsumoto, G. Hirata, H. Takakura, H. Okamoto, and Y. Hamakawa, *J. Appl. Phys.* **67**, 6538 (1990).
- ²⁵W. B. Jackson and N. M. Amer, *Phys. Rev. B* **25**, 5559 (1982).
- ²⁶W. K. Chu, J. W. Mayer, and M. A. Nicolet, *Backscattering Spectrometry* (Academic, Orlando, FL, 1978).
- ²⁷E. Rauhala, *Nucl. Instrum. Methods Phys. Res. B* **12**, 447 (1985).
- ²⁸L. R. Doolittle, *Nucl. Instrum. Methods Phys. Res. B* **9**, 344 (1985).
- ²⁹G. Vizkelethy, *Nucl. Instrum. Methods Phys. Res. B* **45**, 1 (1990).
- ³⁰A. Matsuda, T. Yamaoka, S. Wolff, M. Koyama, Y. Imanishi, H. Kataoka, H. Matsuura, and K. Tanaka, *J. Appl. Phys.* **60**, 4025 (1986).
- ³¹R. Tsu, P. Menna, and A. H. Mahan, *Sol. Cells* **21**, 189 (1987).
- ³²N. F. Mott and E. A. Davis, *Electronic Processes in Non-Crystalline Materials* (Clarendon, Oxford, 1970).
- ³³J. Robertson, *Philos. Mag. B* **66**, 615 (1992).
- ³⁴F. Giorgis, F. Giuliani, C. F. Pirri, A. Tagliaferro, and E. Tresso, *Appl. Phys. Lett.* **72**, 2520 (1998).
- ³⁵Y. Katayama, K. Usami, and T. Shimada, *Philos. Mag. B* **43**, 283 (1981).
- ³⁶S. Liedtke, K. Lips, M. Bort, K. Jahn, and W. Fuhs, *J. Non-Cryst. Solids* **114**, 522 (1989).
- ³⁷R. A. C. M. M. van Swaaij, A. J. M. Bernsten, W. G. J. H. M. van Sark, H. Herremans, J. Bezemer, and W. F. van der Weg, *J. Appl. Phys.* **76**, 251 (1994).
- ³⁸B. Ranby and J. F. Rabek, *Photodegradation, Photo-oxidation and Photostabilization of Polymers* (Wiley, Bristol, 1975).
- ³⁹A. Helmold, P. Hammer, J. U. Thiele, K. Rohwer, and D. Meissner, *Philos. Mag. B* **72**, 335 (1995).
- ⁴⁰Rusli, J. Robertson, and G. A. J. Amaratunga, *Diamond Relat. Mater.* **6**, 700 (1997).
- ⁴¹J. Robertson, *Philos. Mag. B* **76**, 335 (1997).
- ⁴²W. Lormes, M. Hundhausen, and L. Ley, *J. Non-Cryst. Solids* **227–230**, 570 (1998).
- ⁴³R. A. Street, *Hydrogenated Amorphous Silicon* (Cambridge University Press, Cambridge, 1991).
- ⁴⁴S. V. Chernyskov, E. I. Terukov, V. A. Vassilyev, and A. S. Volkov, *J. Non-Cryst. Solids* **134**, 218 (1991); V. A. Vassilyev, A. S. Volkov, E. Musabekov, E. I. Teruhov, S. V. Chernyskov, and Y. M. Shernyakov, *ibid.* **114**, 507 (1989).
- ⁴⁵L. R. Tessler and L. R. Cirino, *Mater. Res. Soc. Symp. Proc.* **420**, 783 (1996).
- ⁴⁶D. Dasgupta, F. Demichelis, C. F. Pirri, and A. Tagliaferro, *Phys. Rev. B* **43**, 2131 (1991).
- ⁴⁷S. Liu, S. Gangopadhyay, G. Sreenivas, S. S. Ang, and H. A. Naseem, *Phys. Rev. B* **55**, 13020 (1997).
- ⁴⁸P. Reinke, W. Jacob, and W. Moeller, *J. Appl. Phys.* **74**, 1354 (1993).
- ⁴⁹J. Cernogora, *Phys. Status Solidi B* **201**, 303 (1997).
- ⁵⁰N. Mutsukura, S. Inoue, and Y. Machi, *J. Appl. Phys.* **72**, 43 (1992).
- ⁵¹F. Demichelis, F. Giorgis, C. F. Pirri, and E. Tresso, *Philos. Mag. B* **71**, 1015 (1995).
- ⁵²F. Demichelis, C. F. Pirri, E. Tresso, and T. Stapinski, *J. Appl. Phys.* **71**, 5641 (1992).
- ⁵³H. Herremans, W. Gravendonk, R. A. C. M. M. van Swaaij, W. G. J. H. M. van Sark, A. J. M. Berntsen, W. M. Arnold Bik, and J. Bezemer, *Philos. Mag. B* **66**, 787 (1992).
- ⁵⁴T. Fujii, M. Yoshimoto, T. Fuyuki, and H. Matsunami, *Jpn. J. Appl. Phys., Part 1* **36**, 289 (1997).
- ⁵⁵A. Grill, V. Patel, and B. S. Meyerson, *J. Mater. Res.* **5**, 2531 (1990).